On the influence of curvature and torsion on turbulence in helically coiled pipes

2014 J. Phys.: Conf. Ser. 501 012025

(http://iopscience.iop.org/1742-6596/501/1/012025)

Journal of Physics: Conference Series **501** (2014) 012025 doi:10.1088/1742-6596/501/1/012025

On the influence of curvature and torsion on turbulence in helically coiled pipes

M Ciofalo [+]**, M Di Liberto and G Marotta**
Dipartimento DEIM, Università degli Studi di Palermo, Italy
[+] Corresponding author; email michele.ciofalo@unipa.it, tel. +39 320 43 95 854

Abstract. Turbulent flow and heat transfer in helically coiled pipes at Re_τ=400 was investigated by DNS using finite volume grids with up to 2.36×10^7 nodes. Two curvatures (0.1 and 0.3) and two torsions (0 and 0.3) were considered. The flow was fully developed hydrodynamically and thermally. The central discretization scheme was adopted for diffusion and advection terms, and the second order backward Euler scheme for time advancement. The grid spacing in wall units was ~3 radially, 7.5 circumferentially and 20 axially. The time step was equal to one viscous wall unit and simulations were typically protracted for 8000 time steps, the last 4000 of which were used to compute statistics. The results showed that curvature affects the flow significantly. As it increases from 0.1 to 0.3 the friction coefficient and the Nusselt number increase and the secondary flow becomes stronger; axial velocity fluctuations decrease, but the main Reynolds shear stress increases. Torsion, at least at the moderate level tested (0.3), has only a minor effect on mean and turbulence quantities, yielding only a slight reduction of peak turbulence levels while leaving pressure drop and heat transfer almost unaffected.

1. Introduction and literature review on flow and heat transfer in curved pipes and coils

1.1. Problem definition and notation

Curved pipes are commonly encountered in engineering equipment involving fluid flow and heat transfer. For example, helical coils are widely used for heat exchangers and steam generators in power plant because they easily accommodate thermal expansion and may exhibit higher heat transfer rates than straight pipes [1-3].

Figure 1 shows a schematic representation of a single coil of a helical pipe (computational domain) with its main geometrical parameters: coil radius c, pipe radius a, and coil pitch $2\pi b$. Inner and outer sides are indicated by "*I*" and "*O*", respectively; top and bottom sides by "*T*" and "*D*", respectively.

The dimensionless curvature and torsion can be defined as:

$$\delta = \frac{a}{c} \tag{1}$$

$$\lambda = \frac{b}{c} \tag{2}$$

Instead of the torsion λ, the torsion parameter τ (dimensionally length^{-1}) is sometimes used:

$$\tau = \frac{b}{\left(c^2 + b^2\right)} \tag{3}$$

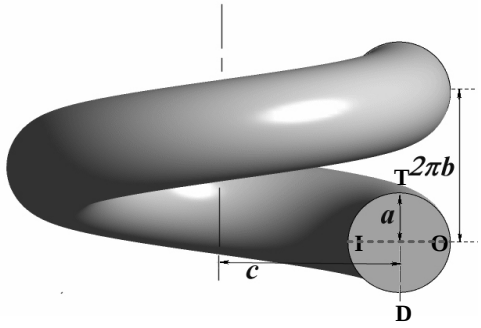

Figure 1. Schematic representation of a helical pipe with its main geometrical parameters: *a*, pipe radius; *c*, coil radius; $2\pi b$, coil pitch. The inner (*I*), outer (*O*), top (*T*) and bottom (*D*) sides of the curved duct are indicated.

Helical coils reduce to curved (toroidal) pipes when λ=0. Several studies, e.g. [4, 5], show that coil torsion λ has only a higher order effect on the flow and on global quantities, such as the friction coefficient, with respect to the first order effect of curvature δ. The effect of curvature is the occurrence of two counter-rotating vortices in the cross section, while the effect of torsion is a loss of symmetry with respect to the equatorial midline *I*-*O*.
Without loss of generality, the duct can be considered as a right-handed helix. The centreline of this helix, i.e. the main axis of the duct, can be parameterized using the angle of rotation φ as:

$$\mathbf{P}(\varphi) = c\cos\varphi\cdot\mathbf{i} + c\sin\varphi\cdot\mathbf{j} + b\varphi\cdot\mathbf{k} \tag{4}$$

where **i**, **j** and **k** are the unit vectors of a Cartesian reference frame (x_1, x_2, x_3), see figure 2.
Germano [4] introduced an orthogonal reference system for helical pipes, based on the helical coordinates *s* (axial), *r* (radial) and θ (azimuthal), with the prescription that θ be measured from a reference azimuth which rotates anticlockwise (for a right-handed helix) as $-\tau s$ (where τ is the torsion parameter defined above). The position of any point inside the helical pipe is given by the vector

$$\mathbf{X} = \mathbf{P}(s) - r\sin(\theta-\tau s)\cdot\mathbf{N}(s) + r\cos(\theta-\tau s)\cdot\mathbf{B}(s) \tag{5}$$

where **T**, **N** and **B** are the unit vectors along the tangential, normal, and binormal directions of the pipe axis **P**(*s*). By expanding **T**, **N** and **B** in terms of the unit vectors **i**, **j** and **k**, and taking account of Eq. (4), Eq. (5) becomes a rule for transforming Germano coordinates into Cartesian ones. Complete direct and inverse transformations [6] are cumbersome and will not reported here.

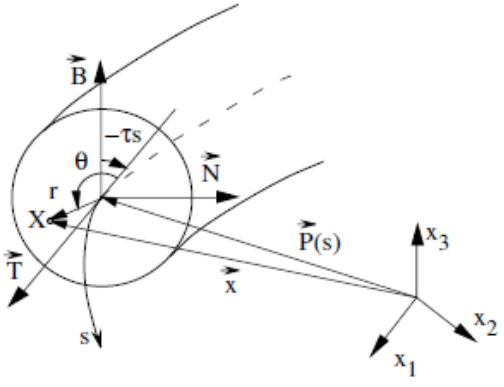

Figure 2. Sketch of the orthogonal helical coordinate system (*s*, *r*, θ), as introduced by Germano [4].

In the present study, as also discussed in section 2.3, instantaneous velocity components and their first- and second-order moments, computed by the code in a Cartesian reference frame, were converted in the Germano coordinate system where they acquire their full physical significance.
In the following, the cross-sectional average of a generic quantity ϕ will be indicated by Φ and its time average by ϕ_{avg} or $\overline{\phi}$, while the fluctuation $\phi-\phi_{avg}$ will be indicated by ϕ' and its root mean square value by ϕ_{rms}. The notation $\langle\phi\rangle$ will be used for the circumferential average of a wall quantity (e.g. the wall shear stress τ_w). The bulk Reynolds number Re will be defined on the basis of the pipe diameter

$2a$ and the time- and cross-section-averaged (bulk) velocity U_{avg} as $\mathrm{Re}=2U_{avg}a/\nu$, ν being the kinematic viscosity of the fluid. The friction-velocity Reynolds number will be defined as $\mathrm{Re}_\tau=u_\tau a/\nu$, where $u_\tau=\left(\langle\overline{\tau}_w\rangle/\rho\right)^{1/2}$ is the friction velocity based on the time- and circumferentially-averaged wall shear stress. Wall scales can be built on the basis of u_τ, i.e. u_τ itself for velocity, ν/u_τ for length, u_τ^2 for Reynolds stresses and turbulence energy, etc.; the corresponding normalized quantities will be denoted by a superscript +. The temperature wall scale will be $T_\tau=\langle\overline{q}''_w\rangle/\left(\rho c_p u_\tau\right)$, $\langle\overline{q}''_w\rangle$ being the time- and wall-averaged heat flux; in this way, the wall scale for heat fluxes, including the turbulent (Reynolds) heat flux $\rho c_p\overline{u_i'T'}$, will be $\langle\overline{q}''_w\rangle=\rho c_p u_\tau T_\tau$. The dimensionless temperature T^+ will be computed as $(T_w\text{-}T)/T_\tau$; note that T^+ vanishes at the wall and is always positive in the bulk flow, provided the wall heat flux q''_w is regarded as positive if entering the fluid and negative otherwise.

The friction velocity u_τ can also be used to define the Large Eddy TurnOver Time (LETOT) a/u_τ, a scale currently used in direct and large-eddy simulations of turbulence to identify the minimum simulation time required for statistical significance. Since the wall time unit is ν/u_τ^2, one LETOT corresponds to a number of wall time units equal to the friction velocity Reynolds number Re_τ [7].

Finally, the inner (tube) side Nusselt number will be defined as:

$$\mathrm{Nu}=\frac{\langle\overline{q}''_w\rangle 2a}{\chi\left(T_w-T_b\right)} \tag{6}$$

where χ is the fluid thermal conductivity and T_b is the bulk fluid temperature. On the basis of the above-mentioned definitions, one also has $\mathrm{Nu}=(2a)/(\chi T_b^+)$.

1.2. Flow field and pressure drop

Flow in curved pipes with zero torsion is characterized by the existence of a secondary circulation in the cross section, caused by the local imbalance between pressure and inertial (centrifugal) forces. The fluid moves towards the outer bend side near the equatorial midplane, returns towards the inner side along two near-wall boundary layers, and then forms two symmetric secondary cells (Dean vortices) having a characteristic velocity scale $U_{avg}\,\delta^{1/2}$. This picture changes only slightly for finite but moderate values of the torsion.

Experimental pressure drop results for a wide range of curvatures and Reynolds numbers were presented by Ito [8], who derived the following correlations for the Darcy-Weisbach friction factor f (four times the Fanning coefficient) in curved pipes ($5\times10^{-4}\le\delta\le0.2$):

$$f=\frac{64}{\mathrm{Re}}\cdot\frac{21.5\cdot\mathrm{De}}{(1.56+\log_{10}\mathrm{De})^{5.73}} \qquad \text{(laminar flow)} \tag{7}$$

$$f=0.304\cdot\mathrm{Re}^{-0.25}+0.029\sqrt{\delta} \qquad \text{(turbulent flow)} \tag{8}$$

in which Re is the bulk Reynolds number and $\mathrm{De}=\mathrm{Re}\,\delta^{1/2}$ is the *Dean number*, which accounts for inertial, centrifugal and viscous effects. Note that Eqs. (7)-(8) do not explicitly contain torsion.

Ito's correlations, although dated, have been confirmed to a notable degree by a large bulk of experimental studies; for example, they agree well with the experiments conducted by Cioncolini and Santini [9] in a broad range of curvatures ($0.027\le\delta\le0.143$) and Reynolds numbers ($\mathrm{Re}\approx10^3\text{-}7\times10^4$).

Several authors attempted to characterize the transition to turbulence in curved pipes. Among computational studies, Di Piazza and Ciofalo [10] presented detailed results on the breakdown of steady laminar flow and the transition to turbulence in closed toroidal pipes having curvatures δ of 0.1 and 0.3. They observed a complex transition scenario, characterized by travelling waves, involving periodic, quasi-periodic and chaotic solutions depending on curvature and Reynolds number. Chaotic flow was obtained for Re>~7000 in the case δ=0.1 and for Re>~8000 in the case δ=0.3.

Three-dimensional numerical simulations of unsteady flow in helical and curved pipes were also presented by Friedrich and co-workers [11, 12]. They compared toroidal and helical pipe results for

Re≈5600 (Re_τ≈230) and δ=0.1. Although the authors performed a statistical processing of the computational results (e.g. by computing Reynolds stress), the case they studied was a time-dependent laminar flow rather than a truly turbulent flow [10].

1.3. Heat transfer

As regards heat transfer, many experimental studies were performed in the 1960s and the 1970s on the average heat transfer rate in curved and helical pipes, e.g. by Seban and McLaughlin [13] and Mori and Nakayama [14]; only some of these investigations explored the influence of the Prandtl number on heat transfer, and very few investigated the local heat transfer rate distribution.

Rogers and Mayhew [15] proposed for the Nusselt number in helical pipes the following correlation:

$$\mathrm{Nu} = 0.023\,\mathrm{Re}^{0.85}\,\mathrm{Pr}^{0.4}\,\delta^{0.1} \tag{9}$$

This formula is basically a curvature correction to the Dittus-Bölter correlation; since it does not contain the pipe torsion, it does not distinguish between planar and helical curved pipes and it does not exhibit the correct asymptotic behaviour for small δ, predicting Nu=0 for straight pipes.

In their experimental study on heat transfer in helical pipes, Xin and Ebadian [16] explored two values of curvature, i.e. δ=0.027 and 0.08, Re from $5\cdot10^3$ to $1.1\cdot10^5$, and three different fluids covering a broad range of Prandtl numbers, i.e. air (Pr=0.7), water (Pr=5), and ethylene glycol (Pr=175). Results for air and water (0.7<Pr<5) were approximated by the following correlation:

$$\mathrm{Nu} = 0.00619\,\mathrm{Re}^{0.92}\,\mathrm{Pr}^{0.4}\left(1+3.455\delta\right) \tag{10}$$

with an RMS deviation of 18% for 0.7<Pr<5, 5×10^3<Re<10^5, 0.0267<δ<0.0884. Even Eq. (10) does not distinguish between planar and helical pipes, but, unlike Eq. (9), it exhibits a reasonable asymptotic behaviour for straight pipes.

2. Models and methods

2.1. Computational mesh

As mentioned above, the computational domain was a single coil of helical pipe, shown in figure 1 for the case δ=0.3. In particular, two curvatures, δ=0.3 and δ=0.1, and two torsions, λ=0.3 and λ=0 (toroidal pipe), were simulated [18]. The finite volume computational grid was hexahedral and multi-block structured; it was characterized by the parameters N_{RAD} and N_θ as shown in figure 3.

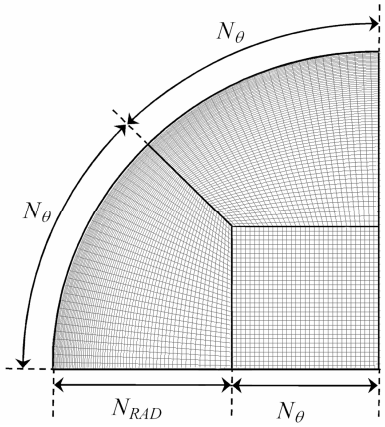

Figure 3. One fourth of the cross section with the computational multi-block hexahedral mesh. The number of cells in the whole cross section is $4N_\theta(N_\theta+2N_{RAD})$.

In the fine grid used for the simulations reported here, the values N_{RAD}=64, N_θ=32 were adopted. With these choices, the cross section was resolved by ~21 000 volumes. In the streamwise direction the domain was discretized by N_S=384 cells for δ=0.3 and by N_S=1152 cells for δ=0.1, so that the total number of control volumes was $N\approx7.86\cdot10^6$ for δ=0.3 and $N\approx2.36\cdot10^7$ for δ=0.1. Geometric refinement was introduced at the wall, with a consecutive cell size ratio of ~1.025 in the radial direction. For Re_τ=400, the first near-wall grid point (volume centre) was at $y^+\approx0.5$ and the viscous sublayer ($y^+\leq11$)

was resolved by 10 grid cells. The Kolmogorov length scale $\Lambda_K=(\nu^3/\varepsilon)^{1/4}$, ε being the dissipation of turbulence energy per unit mass, can be expressed for the present configuration (in the average) as $\Lambda_K=a\mathrm{Re}_\tau^{-1/2}\,\mathrm{Re}^{-1/4}$. For Re_τ=400 and Re ranging from 9450 (δ=0.3) to 11800 (δ=0.1), it can be shown that, in wall units, $\Lambda_K^+ \simeq 2$ so that the fine mesh provides a resolution of ~0.5Λ_K to 2.5Λ_K radially, ~10Λ_K streamwise and ~5Λ_K or less spanwise (of course, the largest values are attained near the wall).

2.2. Numerical methods

Simulations were conducted by the ANSYS CFX 13 code [17]. It uses a finite volume approach, a co-located (non-staggered) grid layout and a coupled technique, which simultaneously solves all the transport equations in the whole domain. The linearized system of equations is preconditioned in order to reduce all the eigenvalues to the same order of magnitude. An algebraic multi-grid solver reduces the low frequency error, converting it to a high frequency error at the finest grid level; this results in a great acceleration of convergence.

To simulate fully developed flow and heat transfer, periodic boundary conditions were imposed at inlet-outlet, and no slip conditions for the velocity at the wall. A uniform source term was added to the RHS of the axial momentum equation as the driving force per unit volume balancing pressure drop.

At walls, a constant wall temperature T_w was imposed. A local energy source term was applied to compensate the wall heat flux. Taking account of the definition of the Nusselt number based on the bulk temperature T_b, this local source term must be proportional to the local axial velocity. With this treatment, the bulk temperature and the Nusselt number tend to stable values once a statistically steady state is reached. The Prandtl number was set to 0.86 (representative of saturated water at 58 bar).

Simulations were protracted for ~20 LETOT's a/u_τ, the last 10 of which were used to build averages and statistics, including RMS temperature fluctuations and turbulent heat fluxes. The time step Δt was chosen equal to one wall time unit ν/u_τ^2, so that one LETOT was resolved by Re_τ=400 time steps and a typical simulation included 8000 time steps. The resulting Courant number was less than 1 almost everywhere in all cases; this time discretization is sufficient to capture most of the turbulent variations.

2.3. Post-processing

Simulations were conducted in a Cartesian reference frame (x, y, z). Instantaneous velocities, pressure and temperature on 8 equally spaced cross sections of the pipe were stored at each time step.

The subsequent post-processing (by purpose written Fortran code) included the following phases:

a. interpolating all quantities on a local 2-D polar grid (r, θ) (100 radial nodes, selectively refined towards the wall, and 180 circumferential nodes were used);
b. projecting all velocity components onto the Germano reference frame (s, r, θ);
c. computing time averages and time statistics to obtain velocity fluctuations and Reynolds stresses;
d. further regularizing all the statistics by averaging them over the 8 cross sections stored.

3. Results

3.1. Power spectra

Figure 4 reports spectra of the axial velocity u_s for δ=0.3, λ=0.3. They were computed in the frequency domain for two points located on the equatorial midline of a cross section in the outer and inner bend regions, respectively, at a dimensionless distance from the wall y^+=20. The abscissa is the frequency f^+, normalized by the viscous frequency scale u_τ^2/ν which is the reciprocal of the time step $\Delta t=\nu/u_\tau^2$ (see section 1.1). Therefore, spectra necessarily exhibit a computational cutoff (indicated in the figures) at $f^+_{\max}=(1/2)(\Delta t^+)^{-1}$=0.5. The Kolmogorov length scale $\Lambda_K=a\mathrm{Re}_\tau^{-1/2}\mathrm{Re}^{-1/4}$ (see section 2.1) corresponds to a dimensionless frequency $f_K^+=(1/2)(U_{avg}/\Lambda_K)/(u_\tau^2/\nu)\approx$2.88, also indicated in the figures. The spectrum for the outer bend side, figure 4(a), exhibits a fairly developed inertial subrange with slope -5/3 extending over about one decade. This is followed by a sharp fall at $f^+\approx$0.1, well below the computational cutoff. This suggests that energy-containing scales are sufficiently resolved by the grid, and are actually far larger than the theoretical Kolmogorov scale deduced above. The spectrum for the inner side, figure 4(b), is different; coherently with the fact that the flow there is almost laminarized, it does not exhibit an inertial subrange and falls at a much lower dimensionless frequency of ~3×10^{-2}.

Similar results are obtained for different values of torsion and curvature. These findings support the view that the grid used is sufficient to resolve all significant structures of the turbulent motion.

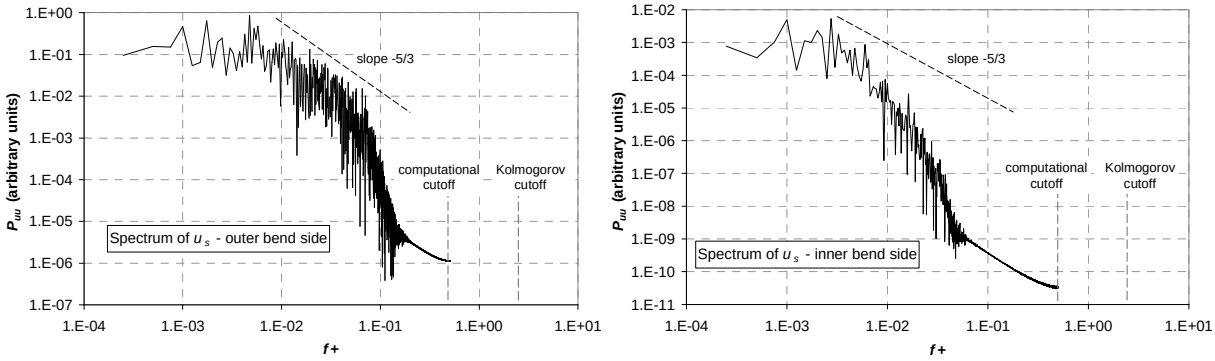

(a) (b)

Figure 4. Power spectra of the axial velocity in the frequency domain for the case δ=0.3, λ=0.3. (a) outer bend region; (b) inner bend region. The dimensionless distance from the nearest wall is y^+=20.

3.2. Influence of torsion

Figure 5 compares, for curvature δ=0.3 and torsion λ=0.3 (helical pipe – solid lines) or λ=0 (toroidal pipe – broken lines), radial profiles of time-averaged streamwise velocity $u_{savg}{}^+$, time mean temperature $T_{avg}{}^+$, total turbulence energy k^+ and axial-radial Reynolds shear stress, all expressed in wall units, along the two orthogonal diametric lines (*I-O* and *T-D*) indicated in figure 1. Note that throughout this paper the cross section is assumed to be viewed from upstream, so that (see figure 1) the inner bend side (*I*) is on the left, while the outer bend side (*O*) is on the right.

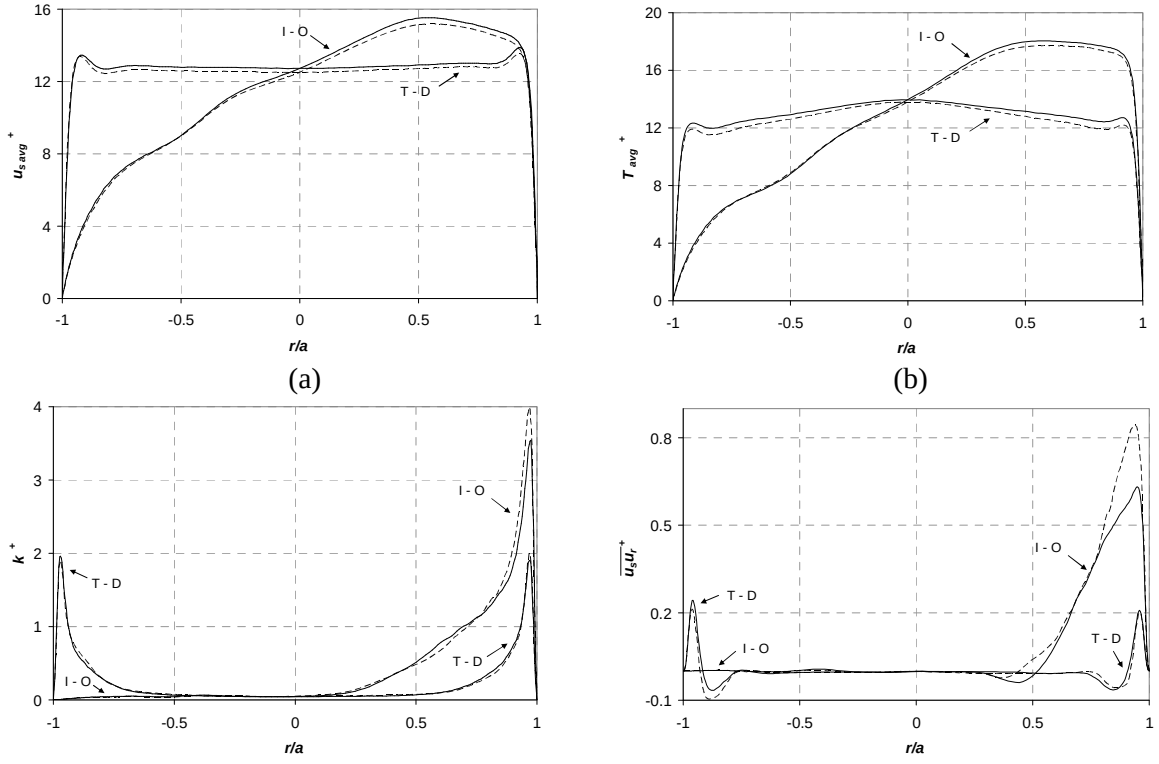

(a) (b)

(c) (d)

Figure 5. Radial profiles of (a) $u_{savg}{}^+$, (b) $T_{avg}{}^+$, (c) k^+ and (d) $\overline{u_s u_r}^+$ (in wall units), along the diametric lines *I-O* and *T-D*, for δ=0.3 and λ=0.3 (solid lines) or λ=0 (broken lines).

Average parameters (u_{savg}^+ and T_{avg}^+) are almost identical in the two cases, while turbulent parameters (k^+ and $u_s u_r^+$) decrease significantly in the presence of torsion, especially on the outer side ("*O*", $r/a>0$) where the turbulence intensity is highest. The reduction is particularly significant (20-25%) for the tangential Reynolds-stress.

Figure 6 shows a similar comparison for δ=0.1. Conclusions here are similar to those given above for δ=0.3, with the exception that, for this smaller curvature, the reduction in the peak value of the Reynolds shear stress on the outer bend side induced by torsion is more significant (~30-35%).

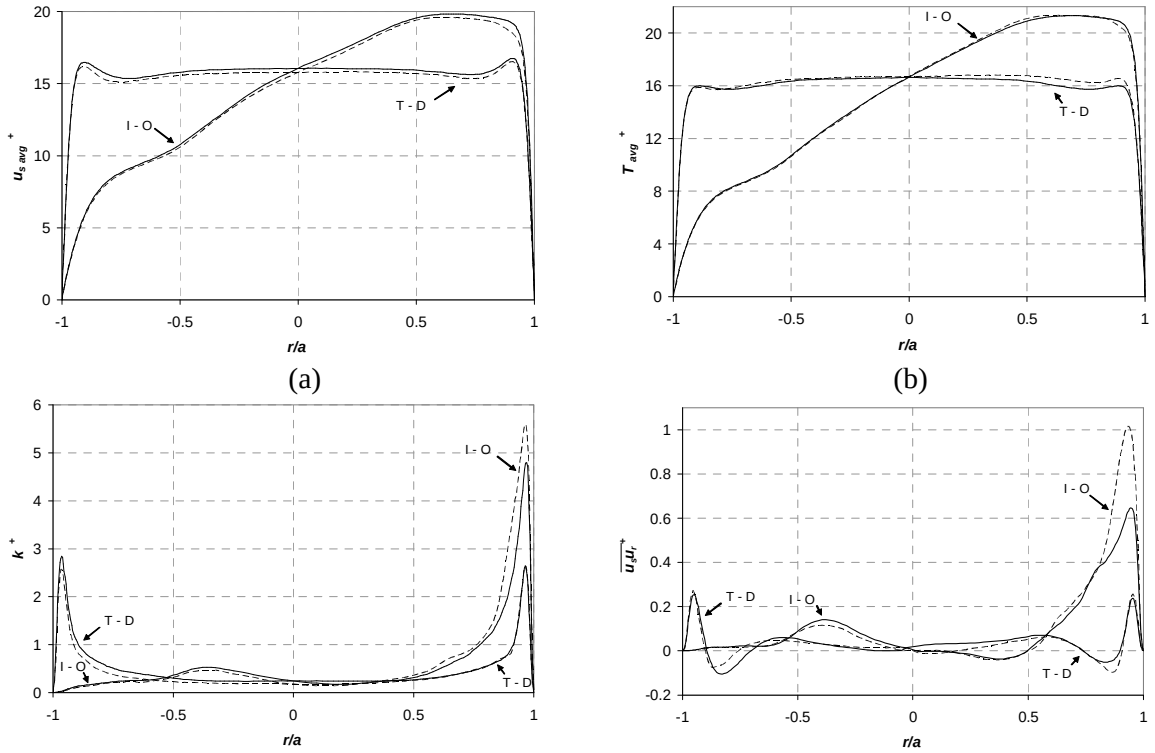

Figure 6. Radial profiles of (a) u_{savg}^+, (b) T_{avg}^+, (c) k^+ and (d) $\overline{u_s u_r}^+$ (in wall units), along the diametric lines *I-O* and *T-D*, for δ=0.1 and λ=0.3 (solid lines) or λ=0 (broken lines).

Figure 7 reports vector plots of the time mean secondary flow for δ=0.3 and λ=0.3 (a) or λ=0 (b).

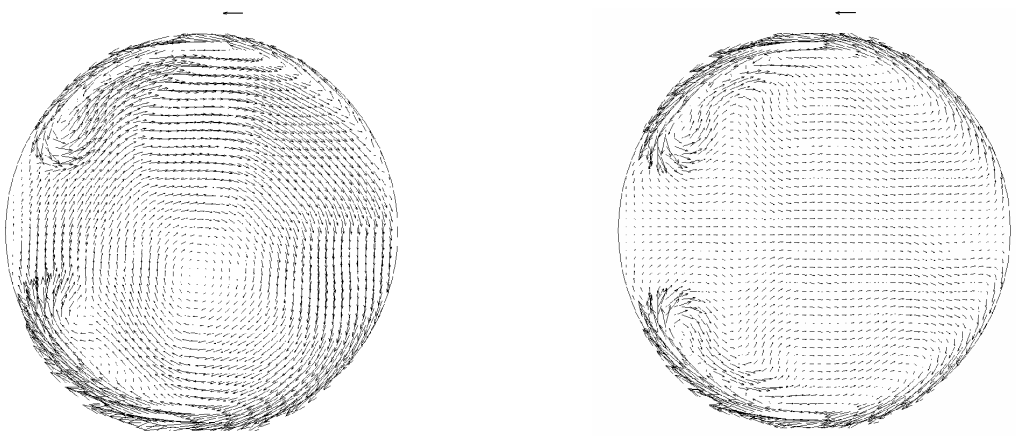

Figure 7. Vector plots of the mean secondary flow for δ=0.3 and λ=0.3 (a) or λ=0 (b). Reference vectors corresponding to u_τ are shown. Inner bend side (*I*) on the left, outer side (*O*) on the right.

The secondary flow for λ=0 (graph b on the right) exhibits the typical Dean circulation pattern, with a broad central region of weak centrifugal flow and two narrow returning (centripetal) secondary flow boundary layers, which end up turning inward and becoming the twin Dean vortices. A similar secondary flow pattern is obtained for λ=0.3 (graph a on the left); here, however, a slight global clockwise rotation of the secondary flow field due to torsion can be noticed, with a loss of the exact top-down symmetry with respect to the equatorial midplane. A weak clockwise recirculation pattern affecting the whole cross section can be observed, with its centre lying slightly below the midplane.
In the following, only results for the cases with finite torsion will be shown. Except for the small differences highlighted above, the results for the cases with zero torsion are very similar.

3.3. Influence of curvature

Figure 8 reports radial profiles (in wall units) of time-mean streamwise velocity u_{savg}^{+} (a), mean temperature T_{avg}^{+} (b) and rms axial, radial and azimuthal velocity fluctuations u_{srms}^{+}, u_{rrms}^{+}, $u_{\theta rms}^{+}$ (c-d), along the lines *I-O* and *T-D*, for λ=0.3 and δ=0.3 (solid lines) or δ=0.1 (broken lines). As in figures 4 and 5, the inner bend side (*I*) lies on the left and the outer bend side (*O*) on the right.

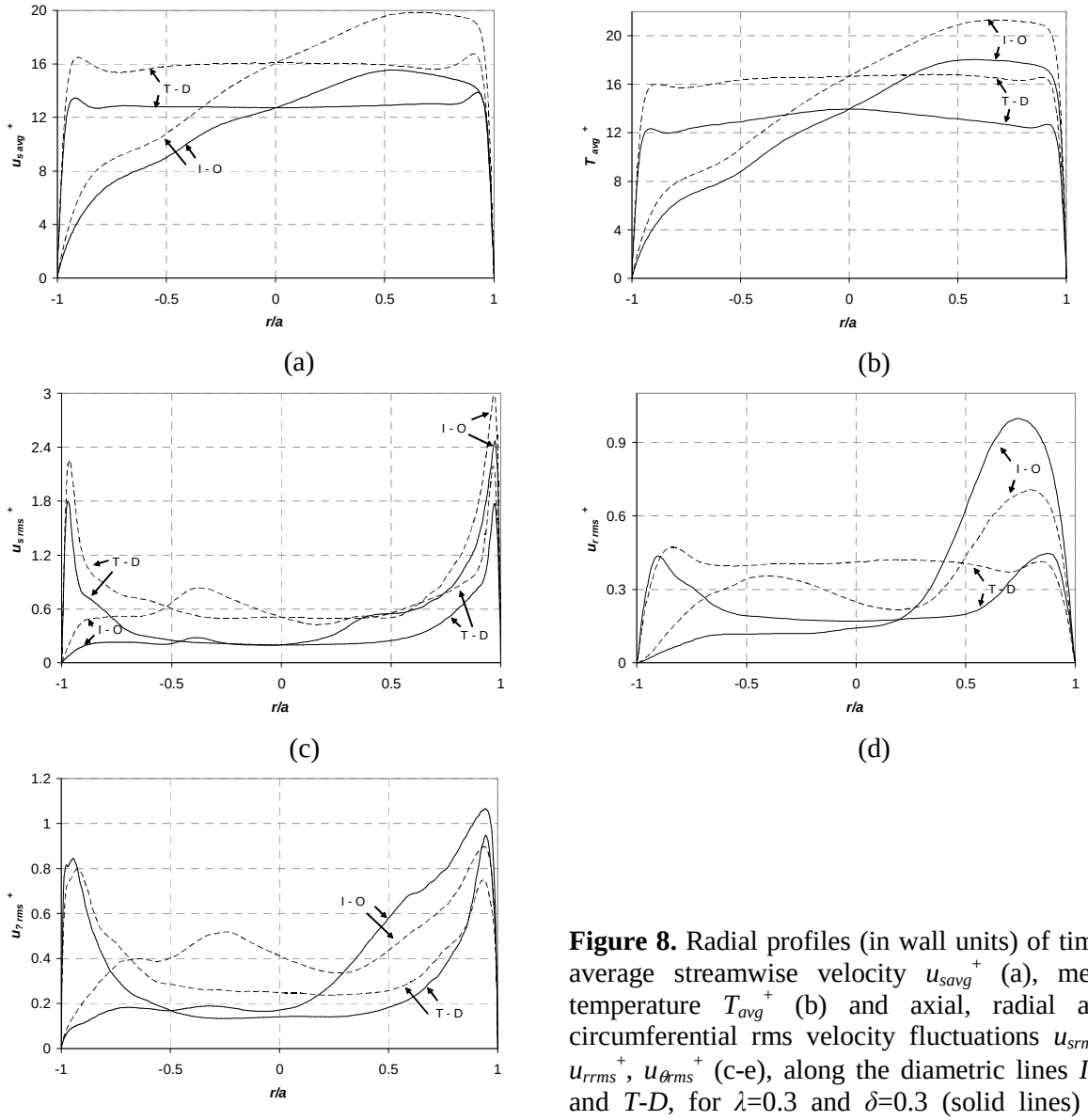

Figure 8. Radial profiles (in wall units) of time-average streamwise velocity u_{savg}^{+} (a), mean temperature T_{avg}^{+} (b) and axial, radial and circumferential rms velocity fluctuations u_{srms}^{+}, u_{rrms}^{+}, $u_{\theta rms}^{+}$ (c-e), along the diametric lines *I-O* and *T-D*, for λ=0.3 and δ=0.3 (solid lines) or δ=0.1 (broken lines).

As the curvature δ increases from 0.1 to 0.3, the mean velocity (graph a) and the mean dimensionless temperature (graph b), once measured in wall units, decrease significantly, which corresponds to an increase both in friction and in heat transfer rates for a given flow rate. As the curvature increases, the axial velocity fluctuation decreases significantly in the central region of the channel and, less markedly, in both the inner and outer near-wall layers. The radial and azimuthal velocity fluctuations decrease in the central region of the channel and in the *I* near wall region, change little in the *T* and *D* near-wall regions, but increase considerably in the *O* near-wall region, where the highest fluctuation levels are observed. Since in pipe and channel flow turbulence is mainly produced in the form of axial fluctuations and is then re-distributed among the other components by pressure-strain rate correlations (redistribution terms), the present findings indicate that curvature enhances the importance of redistribution terms and yields a more isotropic turbulence structure.
Vector plots of the in-plane turbulent (Reynolds) heat flux, for λ=0.3 and for δ=0.3 (a) and δ=0.1 (b), are reported in figure 9. A scale vector of length $\left\langle \overline{q}_w^{"} \right\rangle = \rho c_p u_\tau T_\tau$ is also shown.

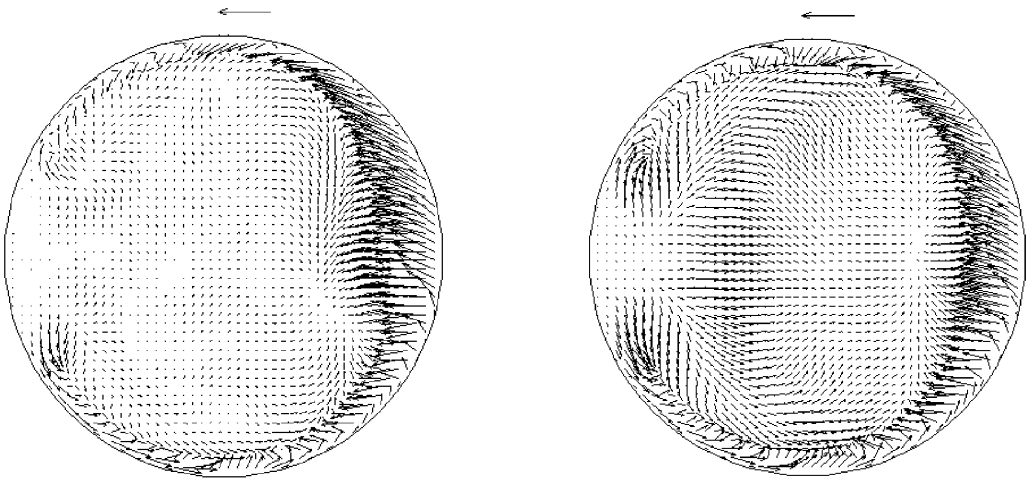

(a) (b)

Figure 9. Vector plots of the turbulent heat flux for λ=0.3 and δ=0.3 (a) or δ=0.1 (b). The scale vector represents the time- and surface-averaged wall heat flux $\left\langle \overline{q}_w^{"} \right\rangle$. Inner bend side (*I*) on the left, outer side (*O*) on the right.

The in-plane turbulent heat flux vector, of components $\rho c_p \overline{u_r' T'}$ (radial) and $\rho c_p \overline{u_\theta' T'}$ (azimuthal), for both cases is large only in the outer region, where its radial component attains peak values well above 1 and contributes significantly to heat transfer from the wall. The turbulent heat flux exhibits negligible values not only near the inner side but also in the Dean vortex regions, which are basically steady structures little affected by turbulent fluctuations.
In the outer bend region the turbulent heat flux is slightly more intense for the higher curvature. On the contrary, in the central and in the Dean vortex regions turbulent fluxes are stronger for the lower curvature, while in the case δ=0.3 these regions are characterized by an almost zero contribution of turbulence to heat transport.

3.4. Wall quantities
Figure 10 represents the distribution of the instantaneous wall shear stress (normalized by its time- and surface-averaged value) over the pipe wall for the four cases.

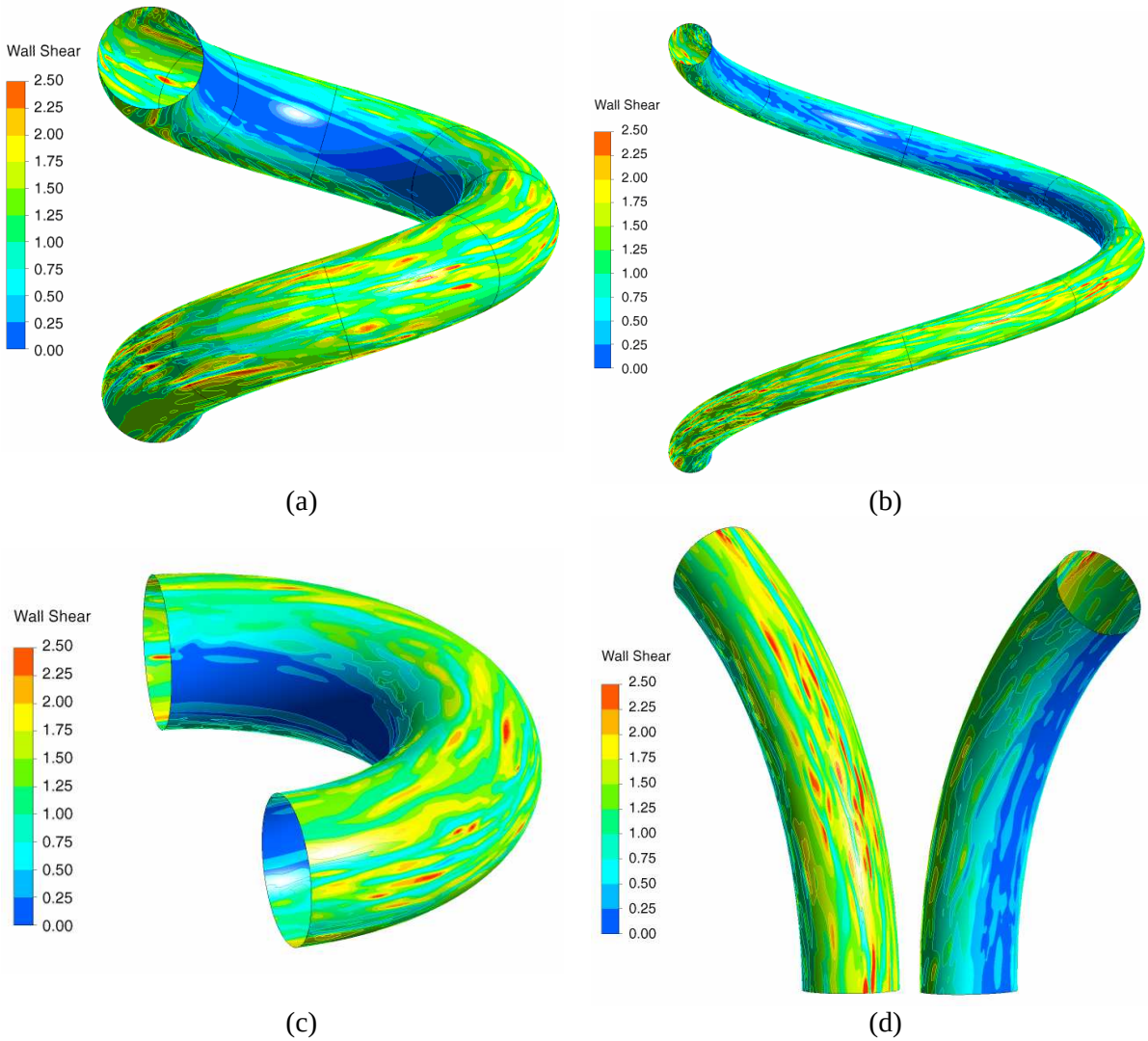

Figure 10. Instantaneous distribution of the wall shear stress τ_w. (a) λ=0.3, δ=0.3; (b) λ=0.3, δ=0.1; (c) λ=0, δ=0.3; (d) λ=0, δ=0.1 (inner and outer side). With reference to the legend on the left, τ_w is normalized by its time- and surface-averaged value $\langle \overline{\tau}_w \rangle$, which is the same for all cases.

All cases exhibit a peculiar pattern. The outer bend side of the pipe, where turbulence levels are high, is covered by a streak pattern not unlike that observed for turbulent flow in straight pipes, and obviously associated with a similar pattern of the near-wall streamwise velocity. The circumferential spacing of the streaks ranges between 100 and 200 wall length units, and their streamwise extent between 500 and 1000. On the other hand, the inner bend side, where turbulence levels are low, exhibits a flat distribution and very low values of the wall shear stress. The difference between the inner and outer sides is more marked for the higher curvature (δ=0.3), and seems to be little affected by torsion.

Similar remarks hold for the following figure 11, which reports the distribution of the instantaneous wall heat flux over the pipe wall for the four cases. Here q'' is normalized by the conductive heat flux, $q''_c=\chi(T_w-T_b)/a$. The outer bend side of the pipe wall is covered by a pattern of thermal streaks, the size and general features of which are similar to those observed for the hydrodynamic streaks in figure 10. The low-turbulence inner bend side exhibits a flat distribution of the local heat flux, which appears to be only slightly higher than the conductive reference heat flux q''_c.

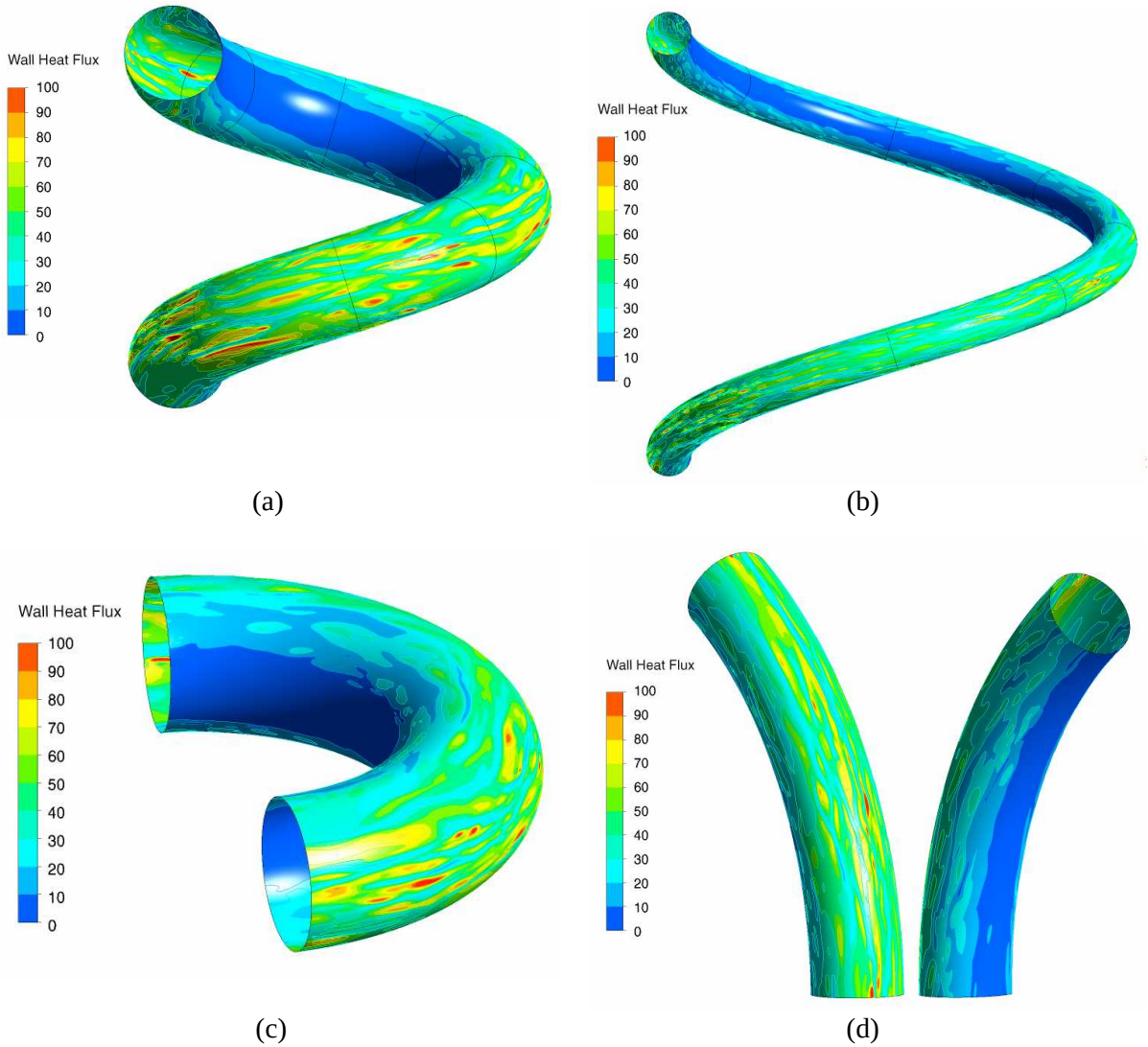

Figure 11. Instantaneous distribution of the wall heat flux q^+ (a) λ=0.3, δ=0.3; (b) λ=0.3, δ=0.1; (c) λ=0, δ=0.3; (d) λ=0, δ=0.1 (inner and outer side). Here q^+ is normalized by the conductive heat flux, $q^+_c=\chi(T_w-T_b)/a$.

4. Conclusions

Direct numerical simulations were performed for fully developed turbulent flow with heat transfer in curved and helical pipes. Four cases, characterized by torsion λ=0.3 or 0 and curvature δ=0.1 or 0.3, were examined. In all cases, the friction velocity Reynolds number was 400 and the Prandtl number was 0.86. The ANSYS CFX 13 computer code was used for all the numerical simulations. Computational grids with up to ~23 million nodes were used; the overall CPU time required for this study was close to 5×10^8 core-seconds.

All cases exhibited a strong asymmetry between the outer bend side, characterized by high turbulence levels, high shear stress and high heat transfer rates, and the inner bend side, characterized by an almost steady flow and by very low levels of wall shear stress and heat transfer. The time-mean flow exhibited a secondary recirculation pattern similar to that observed in high-Reynolds number laminar flow, with the appearance of twin Dean vortices having their centres in the inner region of the cross section.

Increasing the curvature led to a considerable increase of frictional losses and heat transfer rates; it also yielded an increase in turbulence re-distribution, so that peak values of the axial velocity fluctuation decreased whereas peak values of the radial and azimuthal fluctuations increased. Another

effect of increasing the curvature was that fluctuations tended to be confined to the near-wall outer region, while the flow in the core of the pipe became almost laminar.
Torsion, at least at the moderate level tested (0.3), was found to have only a minor effect on mean and turbulence quantities, yielding only a slight reduction of peak turbulence levels while leaving pressure drop and heat transfer almost unaffected. This supports the established practice of using friction and heat transfer correlations which contain only curvature but not torsion.

References

[1] Salimpour M R 2009 Heat transfer coefficients of shell and coiled tube heat exchangers *Exp. Thermal Fluid Science* **33** 203–7.
[2] Yang G and Ebadian M A 1996 Turbulent forced convection in a helicoidal pipe with substantial pitch *Int. J. Heat Mass Transfer* **39** 2015-22.
[3] Di Piazza I and Ciofalo M 2010 Numerical prediction of turbulent flow and heat transfer in helically coiled pipes *Int. J. Thermal Sciences* **49** 653-63.
[4] Germano M 1982 On the effect of torsion in a helical pipe flow *J. Fluid Mech* **125** 1-8.
[5] Chen W H and Jan R 1992 The characteristics of laminar flow in helical circular pipe *J Fluid Mech* **244** 241-56.
[6] Hüttl T J, Chauduri M, Wagner C and Friedrich R 2004 Reynolds-stress balance equations in orthogonal helical coordinates and application *Z. Angew. Math. Mech.* **84** 403-16.
[7] Di Liberto M and Ciofalo M 2013 A study of turbulent heat transfer in curved pipes by numerical simulation *Int. J. Heat Mass Transfer* **59** 112-25.
[8] Ito H 1959 Friction factors for turbulent flow in curved pipes *J. Basic Engineering* **81** 123-34.
[9] Cioncolini A and Santini L 2006 An experimental investigation regarding the laminar to turbulent flow transition in helically coiled pipes *Exp. Thermal Fluid Sci.* **30** 367-80.
[10] Di Piazza I and Ciofalo M 2011 Transition to turbulence in toroidal pipes *J. Fluid Mech.* **687** 72-117.
[11] Hüttl T J and Friedrich R 2001 Direct numerical simulation of turbulent flows in curved and helically coiled pipes *Computers & Fluids* **30** 591-605.
[12] Friedrich R, Hüttl T J, Manhart M and Wagner C 2001 Direct numerical simulation of incompressible turbulent flows *Computers & Fluids* **30** 555-79.
[13] Seban R A and McLaughlin E F 1963 Heat transfer in tube coils with laminar and turbulent flow *Int. J. Heat Mass Transfer* **6** 387-95.
[14] Mori Y and Nakayama W 1967 Study of forced convective heat transfer in curved pipes *Int. J. Heat Mass Transfer* **11** 37-59.
[15] Rogers G F C and Mayhew Y R 1964 Heat transfer and pressure loss in helically coiled tubes with turbulent flow *Int. J. Heat Mass Transfer* **7** 1207-16.
[16] Xin R C and Ebadian M A 1997 The effects of Prandtl numbers on local and average convective heat transfer characteristics in helical pipes *J. Heat Transfer* **119** 467-73.
[17] ANSYS Europe Ltd. 2006 *ANSYS CFX manual*.
[18] Marotta G 2012 *Simulazione numerica diretta della turbolenza in condotti elicoidali* MSc Thesis in Energy and Nuclear Engineering, University of Palermo.